Mesh objective characteristic element length for higher-order finite beam elements

(Article begins on next page)

01 September 2025
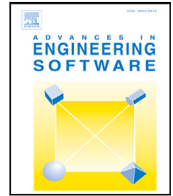
Research paper

Mesh objective characteristic element length for higher-order finite beam elements

J. Shen [a], M.R.T. Arruda [b,*], A. Pagani [a], M. Petrolo [a]

[a] *Mul² Lab, Department of Mechanical and Aerospace Engineering, Politecnico di Torino, Italy*
[b] *CERIS, Instituto Superior Técnico, Universidade de Lisboa, Portugal*

ARTICLE INFO

ABSTRACT

The use of fracture energy regularization techniques can effectively mitigate the mesh dependency of numerical solutions caused by the strain softening behavior of quasi-brittle materials. However, the successful regularization depends on the correct estimation of the crack bandwidth in Finite Element solutions. This paper aims to present an enhanced crack band formulation to overcome the strain localization instability especially for the higher-order elements developed in the framework of Carrera Unified Formulation (CUF). Besides, a modified Mazars damage method incorporating fracture energy regularization is employed to describe the nonlinear damage behavior of the concrete. To evaluate the efficiency of the proposed crack band formulation, three experimental concrete benchmarks are selected for the numerical damage analysis. By comparing numerical and experimental results, the proposed method can guarantee mesh objectivity despite varying finite element numbers and orders, indicating persevered fracture energy consumption within proposed higher-order beam models.

1. Introduction

The mechanical behavior of quasi-brittle materials like concrete typically exhibits strain softening. This phenomenon is characterized by decreasing stress with increasing strain due to the growth and coalescence of microscopic defects. Using Continuum Damage Mechanics (CDM) to model such materials is widely accepted in scientific and engineering communities [1]. Various damage models have been proposed within the CDM framework to describe strength and stiffness degradation. These include isotropic damage models using scalar damage variables [2,3], anisotropic damage models [4], and models coupling damage with plasticity [5,6]. However, a critical issue arises from stress localization, where uniform strain distribution changes into a highly localized one. This localization leads to zero fracture energy dissipation, resulting in ill-posedness and a lack of objectivity in numerical analyses [7]. Consequently, such instability notably causes significant spurious mesh sensitivity in Finite Element (FE) solutions, affecting their accuracy and reliability.

Various regularization techniques have been proposed to restore the objectivity of CDM. One widely adopted approach is based on nonlocal formulations, including integral-type models [8,9] and gradient-type models [10]. The key idea of the nonlocal model is defined as a function of the average strain across a specific representative volume of the material at a given point [11]. However, the implementation

of this method is complex, and determining the appropriate size for the representative volume, empirically associated with the size of the aggregate in concrete, presents a significant challenge. Additionally, spurious boundary effects may occur if the influence of the physical boundaries is not adequately considered [8].

An alternative method involves adjusting the constitutive law based on the width of the localized band, which is significantly influenced by the FE mesh in numerical analyses. This approach, known as the crack band model or fracture energy regularization technique, was first proposed by [12]. This method calculates fracture energy as the product of dissipation density and the localized bandwidth [13]. Dissipation density, the energy dissipated per unit volume, represents the area under the stress–strain curve. In standard CDM, fracture energy tends to zero as the FE mesh becomes finer, resulting in spurious mesh size dependency. Thus, the objective of the crack band model is to preserve fracture energy by rescaling the post-localized portion of the stress–strain law using a crack bandwidth. A vital advantage of this model is its simplicity in implementation within FE software.

A critical aspect of the crack band model is determining the crack bandwidth, also called the characteristic element length (l_c). This parameter is strongly related to various finite element characteristics in numerical simulations. As reviewed in [13], l_c is influenced by factors such as the type of element used (triangles or quadrilaterals), the order

---

of element approximation (linear or quadratic), the integration scheme (specifically, the number of integration points), and the alignment of the crack band with the FE mesh. Therefore, the first category of methods for estimating l_c is based on the element area or volume [12,14] to consider the mesh size. Some coefficients are introduced to evaluate the influence of other aspects, such as mesh shape and element order in [15]. While this method is straightforward, it does not apply to elements with arbitrary shapes, promoting some mesh sensitivity.

Therefore, Oliver [16] proposed two more robust methods capable of accommodating irregular mesh shapes. Physically, the l_c from one of them is characterized by measuring the distance between boundary edges of the element in the crack normal direction at each Gaussian point. The other one calculates the distance between the two most distant midpoints on the element edge in the crack direction at the midpoint of an isoparametric element. However, these methods have only been validated for two-dimensional (2D) elements with linear interpolation functions. A discontinuity of the first Oliver's method was observed and then solved by Govindjee in [17], making it suitable for linear three-dimensional (3D) elements. Govindjee's approach measures the distance between the two most distant corner nodes of an element in the crack normal direction, physically akin to the projection method proposed by [18]. Building on these concepts, [19] introduced a modification, offering an improved way that calculates the maximum projection of midpoints on the element edge along the crack normal direction to determine l_c.

The methods above effectively address the influences of element size, shape, and mesh alignment, yet they are primarily limited to linear elements. For higher-order elements with more complex interpolation functions, strain softening tends to localize within parts of the element, leading to concurrent softening and unloading within the same element. This phenomenon occurs because the strain field becomes non-uniform using quadratic interpolation functions, as reported in [13,20]. Consequently, employing the earlier methods in such scenarios can overestimate l_c. Therefore, it is suggested to introduce a parameter that accounts for the integration scheme and element order in one-dimensional (1D) and 2D analyses [13,20].

Currently, the efficiency of 1D higher-order beam models based on Carrera Unified Formulation (CUF) [21–23] attract significant interest in structural analysis [24,25]. CUF provides a structural theory framework that enables the derivation of variable kinematic models without relying on ad hoc assumptions. CUF-based beam models derive the 3D displacement field by employing various expansion functions across the beam, utilizing the Finite Element Method (FEM) for solutions [26,27]. Such beam models achieve quasi-3D results while preserving the efficiency of 1D beam models. The estimation of l_c in these models starts with the cubic root of small volumes subdivided according to the element order, as detailed in [28–30]. However, this initial approach, which requires a correlation between the beam element size and the cross-sectional mesh size, can limit the capabilities of 1D-CUF models. To address this limitation, [31] proposed a robust method inspired by [19], achieving mesh-independent results in reinforced concrete structures [32]. Despite this improvement, element order sensitivity remains challenging, as reported in [31].

In this context, the present work aims to develop an updated calculation method for l_c to mitigate the element order sensitivity in 1D-CUF FE models. This new method builds upon Govindjee's approach [17] and incorporates a parameter that accounts for element order inspired by the methodology proposed by [20]. By introducing this parameter, the proposed method ensures comprehensive consideration of the mesh characteristics of 1D-CUF models. An isotropic damage model, based on CDM, is utilized in conjunction with the proposed l_c calculation. Once the proposed l_c resolves the mesh size dependency and element order sensitivity, it is expected to see its successful use in various damage models. The novelty of this research lies in enhancing the crack band model for 1D-CUF models, thereby maximizing their computational efficiency and numerical accuracy.

This paper begins with a concise introduction to the higher-order beam theory based on CUF. Then, a modified Mazars damage model with fracture energy regularization technique, having been verified by [14,31], is briefly introduced to capture the damage behavior of the material. Subsequently, the proposed calculation method for l_c is presented in detail, along with a comparative analysis against the previous method detailed in [31]. To validate the effectiveness of the proposed method for l_c, three examples from experimental tests are selected for numerical analysis. Finally, the paper concludes with significant findings from the analysis and discussions.

2. Unified higher-order structural theories and beam finite elements

This section briefly introduces higher-order beam theories based on CUF and its finite element implementation. As described in [33], the 3D displacement field in 1D beam models is represented by Eq. (1), utilizing expansion functions denoted as F_τ.

$$\mathbf{u}(x,y,z) = F_\tau(x,z)\mathbf{u}_\tau(y), \qquad \tau = 1,2,\ldots\ldots,M \tag{1}$$

where y represents the longitudinal axis of the beam, while x and z correspond to the cross-sectional coordinates; $\mathbf{u}_\tau$ signifies the displacement field along the length of beam; the subscript τ denotes a summation over terms, and M represents the number of terms in the polynomial expansions. Various choices for F_τ exist, including Taylor and Lagrange expansions. Further details are available in [33].

This work employs 2D Lagrange-like polynomials to describe cross-sectional kinematics. This approach can handle arbitrary cross-sections via isoparametric transformation, and the unknowns from polynomials represent pure displacements in numerical modeling. Based on the order of Lagrange expansions, the options typically include linear Lagrange elements with four nodes (L4), quadratic elements with nine nodes (L9), and cubic elements with sixteen nodes (L16). In this study, we employ L9 elements; hence, the expression for one L9 element is provided as an example in Eq. (2).

$$F_\tau = \frac{1}{4}\left(r^2 + rr_\tau\right)\left(s^2 + ss_\tau\right), \quad \tau = 1,3,5,7$$

$$F_\tau = \frac{1}{2}s_\tau^2\left(s^2 + ss_\tau\right)\left(1 - r^2\right) + \frac{1}{2}r_\tau^2\left(r^2 + rr_\tau\right)\left(1 - s^2\right), \quad \tau = 2,4,6,8 \tag{2}$$

$$F_\tau = \left(1 - r^2\right)\left(1 - s^2\right), \quad \tau = 9$$

where (r,s) are the normalized coordinates, while (r_τ, s_τ) represent the normalized coordinates of each node τ.

By applying the FEM to the generalized displacements $\mathbf{u}_\tau$ using the shape function $N_i(y)$, the displacement field as expressed in Eq. (1) can be reformulated as follows:

$$\mathbf{u}(x,y,z) = F_\tau(x,z)N_i(y)\mathbf{u}_{\tau i}, \qquad i = 1,\ldots,N_{NE} \tag{3}$$

where N_{NE} is the number of nodes per beam element, and $\mathbf{u}_{\tau i}$ is the nodal displacement vector, which includes unknown variables. In this FE LE formulation, unlike classical models, the unknown variables of the computational model do not lie on the beam element axis but are placed on the physical surfaces of the body.

The selection of beam elements is entirely independent of the choice of expansion functions. In other words, the order and number of beam and Lagrange elements can be considered input parameters in numerical analysis, highlighting a key advantage of CUF-based models. Common options for beam elements include two-node linear elements (B2), three-node quadratic elements (B3), and four-node cubic elements (B4).

The Principle of Virtual Displacements (PVD) states that the external virtual work (δL_{ext}) is equal to the internal virtual work (δL_{int}). For simplicity, the expressions for external and internal virtual work are presented as follows:

$$\delta L_{ext} = \delta \boldsymbol{u}_{sj}^T \mathbf{F}_{sj} \tag{4}$$

$$\delta L_{\text{int}} = \delta \mathbf{u}_{sj}^{T} \mathbf{K}^{\tau sij} \mathbf{u}_{\tau i} \tag{5}$$

with

$$\mathbf{K}^{\tau sij} = \int_{l} \int_{\Omega} \left[\mathbf{D}(N_j(y) F_s(x, z)) \right]^{T} \mathbf{C} \left[\mathbf{D}(F_{\tau}(x, z) N_i(y)) \right] d\Omega dl \tag{6}$$

where i, j, and τ, s are indexes related to beam shape and cross-sectional expansion functions, respectively. $\mathbf{K}^{\tau sij}$ is a 3×3 fundamental nucleus (FN), which enables the automatic assembly of the element stiffness matrix through the combination of four indexes τ, s, i, and j; l denotes the length of the beam element, and Ω represents the area of cross-section; $\mathbf{C}$ is Hooke's law material matrix; $\mathbf{D}(\cdot)$ is the differentiation operator; $\mathbf{F}_{sj}$ is the external force acting on beam node j and cross-sectional node s.

Then, the governing equation for static problems is derived by applying the PVD and integrating Eq. (4) with Eq. (5). The derived equation can be rewritten as follows:

$$\mathbf{K}^{\tau sij} \mathbf{u}_{\tau i} = \mathbf{F}_{sj} \tag{7}$$

3. Modified Mazars damage model

As described by Mazars in [2], a simple class of isotropic damage models is represented by Eq. (8). This model introduces a scalar damage variable d, which evolves from 0 (indicating intact material) to 1 (signifying fully damaged material), to describe the reduction in material elasticity.

$$\boldsymbol{\sigma} = (1 - d) \mathbf{C} \boldsymbol{\varepsilon} \tag{8}$$

In the framework of Mazars damage model, only positive principle strains contribute to damage evolution. Therefore, a scalar variable named equivalent strain ε_{eq} is defined to regulate the damage variable. This definition allows the conversion of a triaxial state into a uniaxial state. Subsequently, the loading function is defined as follows:

$$f(\boldsymbol{\varepsilon}, \kappa) = \varepsilon_{eq}(\boldsymbol{\varepsilon}) - \kappa \leq 0 \tag{9}$$

where κ is an internal variable. Initially, κ is a constant and equals the elastic strain limit, representing the elastic loading. Following the onset of damage, κ is updated as the ε_{eq}. In the event of unloading, κ becomes a constant again and equals the maximum level of the equivalent strain throughout the load history.

According to [2], the damage variable d in Eq. (8) is defined as a linear combination of the tensile damage d_t and compressive damage d_c, which can be expressed as:

$$d = \alpha_t d_t + \alpha_c d_c \tag{10}$$

where α_t and α_c are the parameters that quantify the respective influences of tension and compression on the total damage. The detailed calculations for α_t and α_c can be found in [14], but it is worth noting that both parameters are less than one, and their sum consistently equals one.

The original damage evolution laws provided by [2] require the calibration of parameters through experimental tests. This part introduces new damage evolution laws derived from the tensile and compressive constitutive laws in the fib Model Code 2020 (fib MC2020) [34]. These laws incorporate a fracture energy regularization technique to prevent zero-energy dissipation and ensure mesh-independent results in numerical modeling.

In the case of tension, a classic exponential softening law is employed, designed to prevent stress from decreasing to zero, thereby ensuring that the damage value never reaches 1.0. This strategy can ensure better convergence. Eq. (11) presents the corresponding damage evolution law. Detailed discussions can be found in [14].

$$d_t = g_t(\kappa_t) = 1 - \frac{\varepsilon_{\text{d}0}}{\kappa_t} \exp\left(\frac{\varepsilon_{\text{d}0} - \kappa_t}{\varepsilon_{\text{tu}} - \varepsilon_{\text{d}0}} \right) \tag{11}$$

where $\varepsilon_{\text{d}0}$ is the limiting elastic strain in a uniaxial state; ε_{tu} is the equivalent ultimate strain for bilinear softening, which controls the slope of the softening and related to the tensile volumetric fracture energy g_{ft}. Its calculation is presented as Eq. (12).

$$g_{\text{ft}} = \frac{G_{\text{ft}}}{l_c} = f_{\text{ctm}} \left(\varepsilon_{\text{tu}} - \varepsilon_{\text{d}0} \right) \tag{12}$$

in which f_{ctm} is the mean tensile strength in a uniaxial state; G_{ft} is the fracture energy dissipated per unit area of a surface due to cracking; l_c is characteristic element length which will be discussed in detail subsequently.

In the case of compression, the uniaxial constitutive law follows the guidelines from fib MC2020 [34]. The concept of residual compressive stress σ_{cres} is introduced to avoid convergence issues. This idea ensures that the stress remains constant once the strain reaches a threshold, termed the residual compressive strain $\varepsilon_{\text{cres}}$. This strategy guarantees that the stress never reduces to zero and the damage value never reaches 1.0. The detailed information can be found in [14]. In this work, the compressive damage evolution law is presented as follows:

$$d_c = g_c(\kappa_c) = \begin{cases} 1 - \dfrac{\left(k \times \eta - \eta^2 \right) f_{\text{cm}}}{(1 + (k-2) \times \eta) E_{\text{cm}} \kappa_c} & \text{if } \kappa_c \leqslant \varepsilon_{\text{c}1} \\[3mm] 1 - \dfrac{f_{\text{cm}}}{E_{\text{cm}} \kappa_c} & \text{if } \varepsilon_{\text{c}1} < \kappa_c \leqslant \varepsilon_{\text{c}2} \\[3mm] 1 + \dfrac{k_1}{E_{\text{cm}}} - \dfrac{k_2}{E_{\text{cm}} \kappa_c} & \text{if } \varepsilon_{\text{c}2} < \kappa_c \leqslant \varepsilon_{\text{cres}} \\[3mm] 1 - \dfrac{\sigma_{\text{cres}}}{E_{\text{cm}} \kappa_c} & \text{if } \varepsilon_{\text{cres}} < \kappa_c \end{cases} \tag{13}$$

with

$$\kappa_c = \frac{\kappa_t}{\nu \sqrt{2}}; \quad k = \frac{1.05 E_{\text{cm}} \varepsilon_{\text{c}1}}{f_{\text{cm}}}; \quad \eta = \frac{\kappa_c}{\varepsilon_{\text{c}1}};$$

$$k_1 = \frac{f_{\text{cm}}}{(\varepsilon_{\text{cu}} - \varepsilon_{\text{c}2})}; \quad k_2 = f_{\text{cm}} + k_1 \times \varepsilon_{\text{c}2} \tag{14}$$

where f_{cm} is the mean compressive strength; E_{cm} is the secant Young's modulus; k, k_1 and k_2 are the parameters from [35] to describe the softening; $\varepsilon_{\text{c}1}$ and $\varepsilon_{\text{c}2}$ are strain parameters that can be taken as 2.0‰ and 2.4‰ from [35], respectively; η is a unidimensional strain ratio provided in [34]. ε_{cu} is the extreme compressive strain for determining the slope of softening part, which is related to the compressive volumetric fracture energy g_{fc} and calculated in Eq. (15).

$$g_{\text{fc}} = \frac{G_{\text{fc}}}{l_c} = f_{\text{cm}} \times \left(\frac{\varepsilon_{\text{cu}} + (\varepsilon_{\text{c}2} - \varepsilon_{\text{c}1})}{2} \right) \tag{15}$$

where G_{fc} is the compressive fracture energy dissipated per unit area of a surface due to crushing.

The tensile and compressive fracture energies are material properties that can be measured from experimental tests. As the element size decreases or finer mesh is adopted in FE, energy dissipation tends towards zero. Therefore, the general idea of fracture energy regularization based on the crack band model is to rescale the stress–strain softening curves. This idea ensures the same energy dissipation per unit area across varying element sizes as shown in Eqs. (12) and (15) in which the fracture energies are converted into volumetric fracture energies, signifying the energy dissipated per unit volume.

4. Estimation for characteristic element length

In FE simulations, the correct estimation of the characteristic length of the element, denoted as l_c, is crucial. Overestimating or underestimating this value can result in inaccurate fracture energy regularization. In general, l_c is viewed as an FE discretization parameter influenced by element characteristics such as the selected element shape,

element size, type of interpolation function, the numerical integration scheme, and element orientation.

Apart from the fundamental approach of calculating the square root of the element area or the cubic root of the element volume, numerous advanced methods have been developed for estimating l_c suitable for general situations. These methods are comprehensively reviewed in [13]. Notably, a method proposed by Govindjee in [17] is particularly significant, as it accounts for the crack band direction and is effective for both 2D and 3D linear elements. The estimation equation proposed by Govindjee [17] is expressed as:

$$l_G(\mathbf{x}) = \left(\sum_{i=1}^{n_c} \left[\frac{\partial N_i}{\partial \mathbf{x}} \beta_i \right] \cdot \mathbf{n}(\mathbf{x}) \right)^{-1} \qquad (16)$$

with

$$\beta_i = \frac{(\mathbf{x}_i - \mathbf{x}_c) \cdot \mathbf{n}(\mathbf{x}) - \beta^{\min}}{\beta^{\max} - \beta^{\min}}$$

$$\beta^{\min} = \min_{i=1,N_{\text{nodes}}} \left\{ (\mathbf{x}_i - \mathbf{x}_c) \cdot \mathbf{n}(\mathbf{x}) \right\} \qquad (17)$$

$$\beta^{\max} = \max_{i=1,N_{\text{nodes}}} \left\{ (\mathbf{x}_i - \mathbf{x}_c) \cdot \mathbf{n}(\mathbf{x}) \right\}$$

where n_c is the number of corner nodes; N_i is the shape function; $\mathbf{x}$ represents the target point, such as Gaussian point (GP); $\mathbf{n}(\mathbf{x})$ is the unit vector in the major principal strain direction; $\mathbf{x}_i$ and $\mathbf{x}_c$ are the corner nodal points and the central point of the same finite element, respectively.

The physical meaning of Govindjee's method is measuring the distance between the two farthest corner nodes of an element in the direction normal to the crack, similar to the projection method. This approach incorporates factors such as the element sizes, shapes, and crack orientation. However, it does not consider the interpolation function and numerical integration scheme. It is important to note that this method is conducted based on the central point of the element, resulting in each GP within the same element having an identical characteristic element length.

Regarding the higher-order displacement approximation functions, [13] identified that strain softening localizes at only some, but not all, GPs within a single element. This phenomenon will lead to the underestimation of l_c if the previous method is employed. Therefore, [20] proposed two parameters to refine Govindjee's approach. The first, α, accounts for the potential effects of higher-order approximation, while the second, γ, serves as an alignment factor. The values of α and γ corresponding to the different element types are suggested in [20]. This method considers nearly all FE characteristics, but its validation was limited to 2D problems. Consequently, these parameters may not be suitable for higher-order beam theories based on CUF.

Building on previous studies, [31] developed a robust approach to estimate the characteristic element length specifically for higher-order beam theories. This strategy enhances an existing method detailed in [19], which evolved from Govindjee's method. According to [19], the characteristic element length is calculated by measuring the distance between the two farthest midpoints of the element edges, oriented normal to the crack direction, in a 2D element that typically has four edges and midpoints. [31] tried to expand this method to 3D space by using the same projection but incorporating additional midpoints because there are eight edges and eight midpoints in one 3D element. Furthermore, [31] subdivided the element according to its order, aiming to address the effects of the interpolation function. Although this method delivers results with accuracy independent of mesh size, it shows higher softening results when quadratic beam elements are employed. This phenomenon was attributed to the mesh sensitivity relative to the element order.

Given the summary above, this study proposes an updated method for estimating the characteristic element length in higher-order beam models to mitigate or eliminate mesh sensitivity associated with element order. The key point of this method is the introduction of

a parameter, α, designed to account for the influence of elements order. This parameter is then employed to modify the l_g derived from Govindjee's method. Since the finite beam elements with cross-sectional expansion are employed in this work, the specific correction for mesh bias is not considered here. The expression of l_c incorporating α is written as follows:

$$l_c = \alpha \times l_g \qquad (18)$$

The computation of α is based on the ratio of the weights of softening GPs to the total weights of all GPs within a beam element. This calculation is illustrated with a simple example in Fig. 1, including the computation for l_g. Fig. 1 depicts a beam element with three nodes. A 9-node Lagrange element is used for each node, leading to the assembly of a 27-node volume element via Lagrange expansion. When a GP undergoes softening, Govindjee's method is applied to project the volume element's corner nodes along the major principal strain direction, denoted as l_g. Subsequently, the condition of each GP is evaluated following a specific rule. The 27 GPs in the volume element are grouped into nine categories, as demonstrated in Fig. 1. Each GP within a group has different weights in Gaussian integration. For instance, the highlighted green group in Fig. 1 contains our interested Gaussian point. Three distinct scenarios are illustrated in Fig. 1: (1) all GPs are softening, resulting in $\alpha = 1$; (2) a sub-element localization pattern is observed, leading to $\alpha = (5/9 + 8/9)/2 = 13/18$; (3) all GPs are either unloading or in elastic loading, setting $\alpha = 0$, and indicating the damage no longer increases or no damage occurs. These adopted values of α were obtained and justified in the work of [13].

**Algorithm 1:** Proposed estimation of the characteristic element length

> **Input** : Beam element with N_{NE} nodes, Lagrange element (LE) with M nodes
>
> **Output:** Characteristic element length $l_c[1 : M, 1 : N_{NE}]$ of all Gaussian points (GPs)

1 Assemble a 3D volume by expanding cross-sections at nodes along the beam element;
2 Obtain and store the 8 corner nodes $\mathbf{X}_i$ of the assembled 3D volume;
3 Group all generated GPs into M sets, each containing N_{NE} points;
4 **for** *each GP* **do**
5   Obtain and store its position $\mathbf{x}$, status, and crack direction $\mathbf{n}(\mathbf{x})$;
6 **end**
7 Initialize an array α of size $M \times N_{NE}$ to zero ($\alpha[1 : M, 1 : N_{NE}] = 0$);
8 **for** $m = 1, M$ **do**
9   Calculate the total weights of GPs in group m, denote this as W_{all};
10   Evaluate the status of each GP in group m;
11   Compute the sum of weights for GPs under softening in group m, denote as W_s;
12   Update the array α for group m using the ratio of W_s to W_{all} ($\alpha[m, 1 : N_{NE}] = W_s/W_{all}$);
13   **for** $n = 1, N_{NE}$ **do**
14   Determine the length $l_g(m, n)$ using Eq. (16);
15   Compute the final characteristic element length $l_c(m, n) = l_g(m, n) \times \alpha(m, n)$.
16   **end**
17 **end**

Once the values of l_g and α have been determined, the proposed method for estimating l_c can be computed using Eq. (18). The procedures for this computation are presented in Algorithm 1, where the l_c of all GPs can be obtained within a given beam element and its corresponding LE. By systematically applying Algorithm 1 to all beam
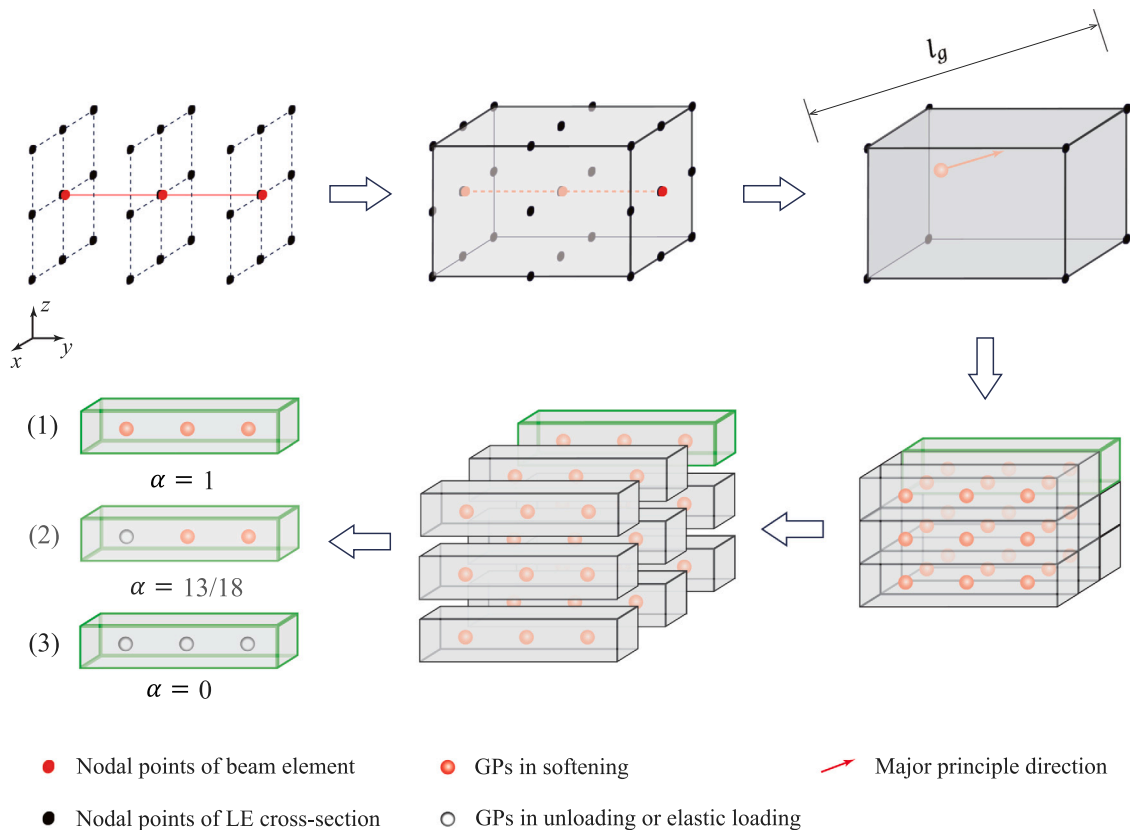
Fig. 1. Illustration of calculations for l_g and α.

elements and their respective LEs, the l_c of all GPs across the entire structural model can be obtained.

Fig. 2 compares the estimated l_c from both the proposed and a previous method, applied to a B3 beam element with a length of 2 mm. The previous method is referred to [31]. An L9 element with a mesh size of 1 mm × 1 mm is utilized for the cross-section. In Fig. 2(a), the l_c calculated by the proposed method is derived from l_g, determined using Govindjee's approach, and subsequently adjusted by the parameter $\alpha = 13/18$. The physical meanings of both Govindjee's method (l_c) and the previous method (l_{cp}) are depicted in Fig. 2(b). The major principle strain direction is defined in terms of azimuthal and elevation angles. The comparison indicates that the l_c values estimated by the previous method are consistently lower than those obtained through the proposed method, regardless of the major principle strain direction.

5. Numerical results

In this section, three numerical benchmark examples from concrete experimental studies are selected to assess the performance of the enhanced crack band model with the proposed estimation method for l_c. Among these examples, one focuses on a reinforced concrete panel that considers the complex behavior between concrete and steel. All numerical models are conducted with the displacement control method.

5.1. The Hassanzadeh test

The first well-known benchmark is the Hassanzadeh test, often used to access concrete damage models. The original experimental campaign was reported in [36]. It is a direct traction test based on a four-side notched plain concrete sample. Fig. 3 indicates the geometric description and loading conditions. The fixed boundary is adopted at the bottom, and monotonic static tension is assigned on the top using

Table 1
Material properties of the Hassanzadeh test.

| Material	Properties	Symbols	Units	Values
Concrete	Young's modulus	E_c	GPa	35.0
	Poisson's ratio	v_c	–	0.2
	Mean compressive strength	f_{cm}	MPa	50
	Tensile strength	f_{ctm}	MPa	3.0
	Fracture energy	G_{ft}	N/m	73.35

displacement control with a maximum value of 0.04 mm. The material properties from [36] are listed in Table 1.

The beam elements are arranged along the thickness of the specimen, as shown in Fig. 4(a). The mesh-independent results have been obtained using B2 and B4 elements using the previous method as discussed in [31]. In this work, the research focus is moved to the B3 elements which demonstrated mesh sensitivity in previous work [31]. Table 2 lists the beam element information for each numerical model. Models 1 and 2, which utilize B2 and B4 elements, are implemented to verify if the proposed method can replicate results comparable to the previous method. The subsequent four models are designed to evaluate whether the proposed method can mitigate the sensitivity of computational results to B3 elements and, by varying the number of B3 elements at the central notch, to confirm if it can produce mesh-independent results. Fig. 4(b) displays the mesh discretization of the cross-section, where each mesh element is a nine-node quadratic Lagrange element (L9) with an individual element size of around 8 mm. All numerical models adopt this same cross-sectional discretization.

Fig. 5 compares load–displacement curves of six models using both a previous method and a novel proposed method. Experimental data is also included for reference. It is evident from Fig. 5(a) that while all models exhibit an initial agreement with the experimental curve, some divergence becomes apparent after the peak load. While minor
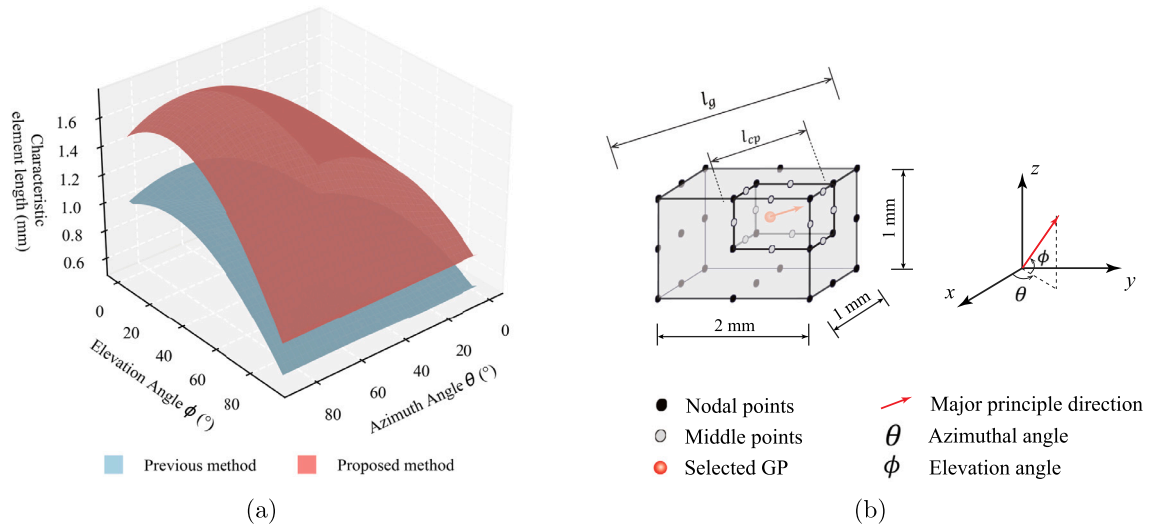
Fig. 2. Comparison of l_c for a B3 element with one L9: (a) l_c from two methods with respect to azimuthal angle and elevation angle; (b) physical meaning of l_g and l_{cp} estimated by [17,31], respectively.
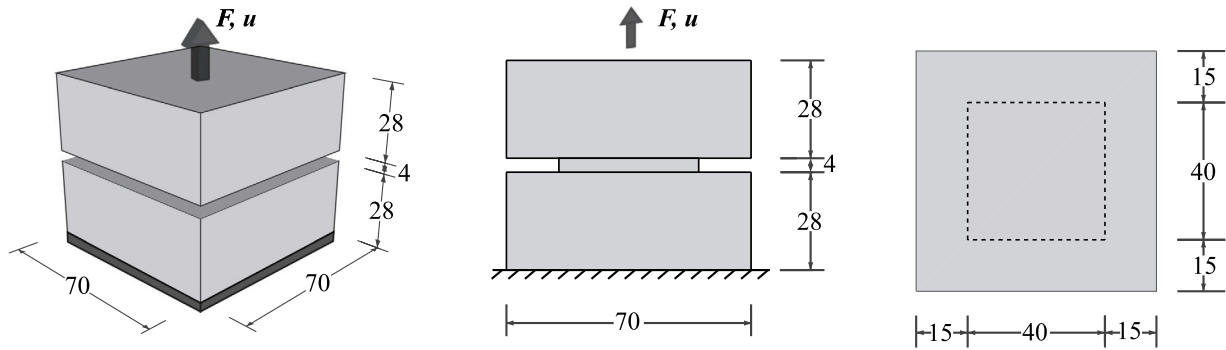
Fig. 3. Geometric information and loading conditions of the Hassanzadeh test.
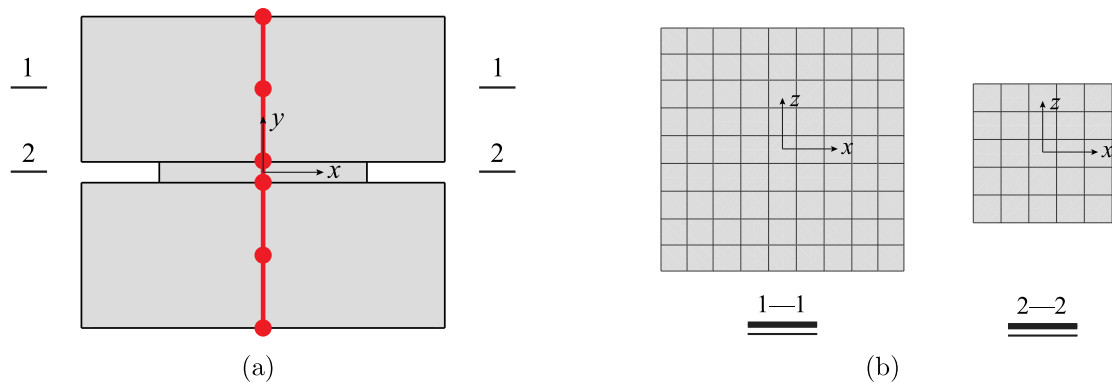
Fig. 4. Discretization of (a) beam elements and (b) cross-sections for the Hassanzadeh test.

Table 2
Model information for the Hassanzadeh test.

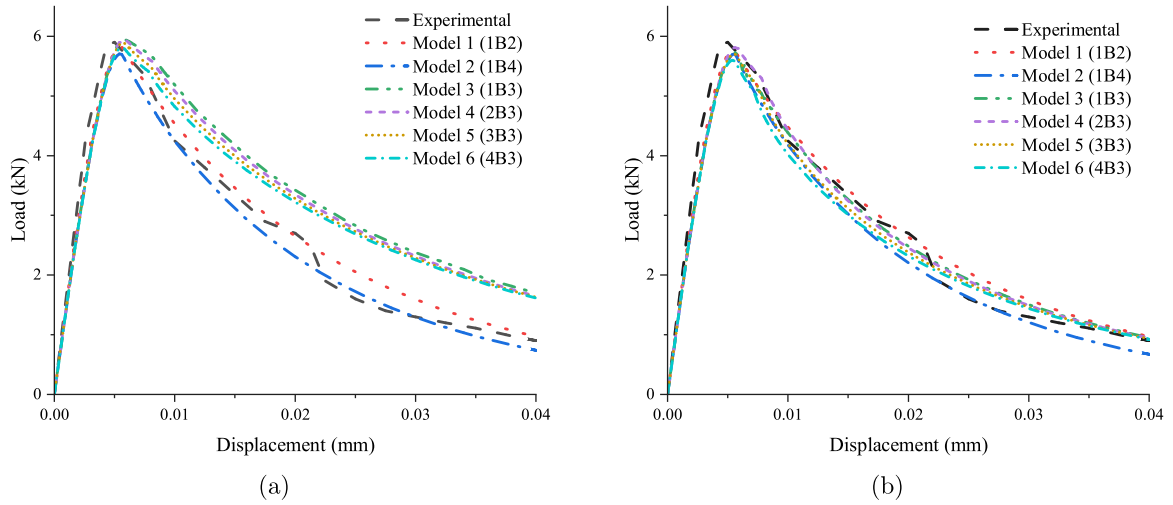| Model No.	Model 1	Model 2	Model 3	Model 4	Model 5	Model 6
Notch elements	1B2	1B4	1B3	2B3	3B3	4B3
Other elements	4B2	2B4	4B3	4B3	4B3	4B3
DoFs	6,498	9,390	11,193	11,919	12,645	13,371

Fig. 5. Comparison of experimental and simulated reaction load–displacement curves from the Hassanzadeh test: with (a) the previous method and (b) the proposed method.

discrepancies between the post-peak curves of Model 1 and Model 2 are observed, both models maintain a close trend to the experimental curve, indicating that their performance is acceptable. The remaining four models, which incorporate B3 elements, show a noticeable deviation in their softening curves from the experimental reference. This non-negligible divergence indicates the earlier method is sensitive to B3 elements as reported in [31]. Despite the observed overestimation, Models 3 to 6 show similar post-peak responses, indicating the previous can mitigate the mesh dependency.

In Fig. 5(b), all models also agree well with the experimental data before the peak load. Moreover, Models 1 and 2 maintain post-peak performances consistent with those observed in Fig. 5(a). Furthermore, the softening curves of Models 3 to 6 have shown significant improvement, closely matching the experimental curve and resembling those of Models 1 and 2. This performance demonstrates that the proposed method can simultaneously mitigate the mesh order sensitivity and mesh size dependency in this case, implying this method may serve as a robust alternative to the existing method.

Fig. 6 displays numerical models' final damage distribution patterns. Models 5 and 6 are omitted due to their similarity to Model 4. The proposed method accurately replicates the damage distributions of the previous method with B2 and B4 elements. However, Model 3 exhibits overestimated damage in the notch area with the former method, as depicted in Fig. 6(c). This miscalculation likely accounts for the excessive softening observed in the result of Model 3 (Fig. 5(a)), resulting from an increased dissipated fracture energy due to expanded damage zones. While increasing the beam element number in the notch refines the damage distribution (see Fig. 6(d)), slightly spurious damage bands still occur, thus affecting model accuracy. In contrast, the proposed method accurately depicts damage localization, primarily within two-thirds of the notch, as shown in Fig. 6(g). This finding aligns with the literature, which suggests strain softening often localizes to two out of three GPs in quadratic beam elements [13]. Further, Fig. 6(h) demonstrates the anticipated damage distribution, with final damage confined to two-thirds of a single B3 element despite using two B3 elements.

The precision of the proposed method is further validated by analyzing the performance at specific GPs, which thoroughly examines the characteristic element length and the corresponding regularized stress–strain relationships. Fig. 7 compares two GPs, one each from Model 1 and Model 2. Despite initial fluctuations in the characteristic element length before peak load, as shown in Fig. 7(a), the two methods exhibit identical values throughout the subsequent loading history. Similarly, the stress–strain curves derived from both methods are highly coincident. This consistency demonstrates the ability of the proposed

Table 3
Material properties of the TPB concrete beam.

Material	Properties	Symbols	Units	Values
Concrete	Young's modulus	E_c	GPa	20.0
	Poisson's ratio	v_c	–	0.2
	Mean compressive strength	f_{cm}	MPa	24.0
	Tensile strength	f_{ctm}	MPa	2.4
	Fracture energy	G_{ft}	N/m	90.0

method to match the precision of the previous method for B2 and B4 elements.

To explain how the proposed method reduces sensitivity to B3 elements, we analyzed the performance of two GPs in Model 3, as depicted in Fig. 8. The positions of these points, which both undergo softening, are indicated in Fig. 8(c). According to Fig. 8(a), the proposed method consistently presents a higher characteristic element length than the previous method, thought they tend to the constant value once the strain deformation increases. This discrepancy accounts for the lower stress–strain softening branches observed with the new method (Fig. 8(b)), as opposed to the elevated softening branches associated with the previous method. The former method's underestimation of l_c results in extra regularization of the stress–strain curves, which in turn causes an overprediction of dissipated fracture energy. This overprediction contributes to the deviation of models incorporating B3 elements from the experimental benchmarks (Fig. 5(a)). Conversely, the proposed method effectively handles this overestimation, aligning the structural performance with experimental observations (Fig. 5(b)). In summary, the proposed method offers accurate damage distribution predictions that are less susceptible to mesh sensitivity or dependency.

5.2. Three point bending test

Another experimental benchmark used in this study is the three-point bending test (TPB) on a notched plain concrete beam, which is an indirect tension test. This test, previously reported in [37], is frequently utilized to evaluate different regularization methods. The beam has a 5 mm wide and 50 mm deep notch at the bottom of the mid-span. Detailed beam dimensions are presented in Fig. 9. The setup includes a simply supported boundary condition and a displacement-controlled load, peaking at 0.5 mm, as shown in Fig. 9. Material properties, referred from [37], are summarized in Table 3.

Beam elements are assigned along the length of the beam, with a denser distribution near the notch, as depicted in Fig. 10(a). Due to the beam's symmetry, a half-structure model is employed for the numerical
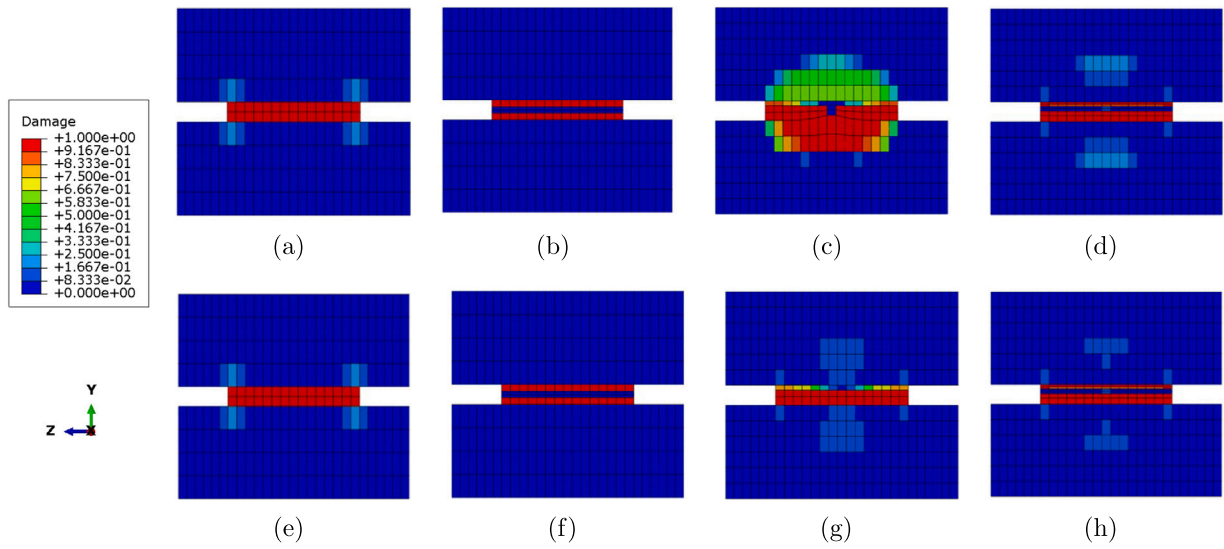
Fig. 6. Final damage distributions of the notched concrete (deformed shape) with previous method from: (a) Model 1 (1B2); (b) Model 2 (1B4); (c) Model 3 (1B3); (d) Model 4 (2B3) and proposed method from: (e) Model 1 (1B2); (f) Model 2 (1B4); (g) Model 3 (1B3); (h) Model 4 (2B3)
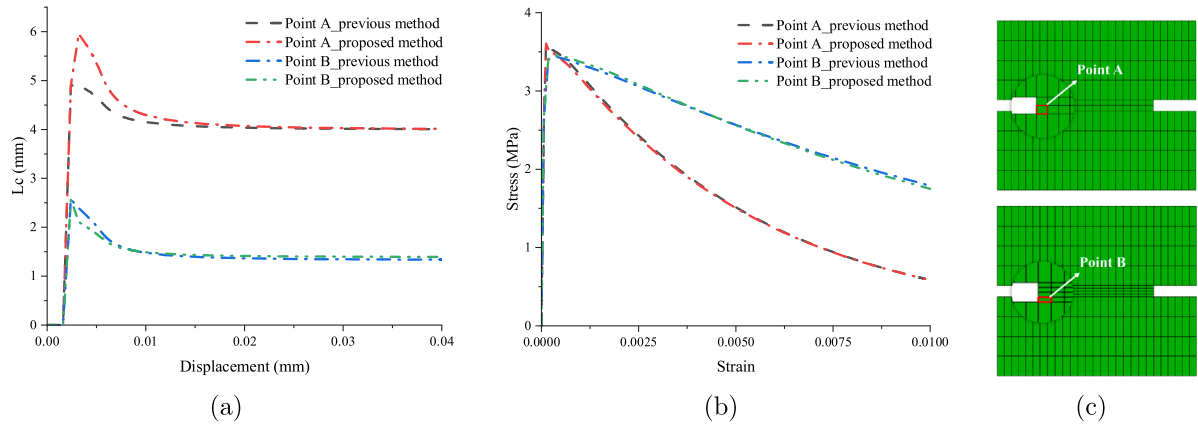
Fig. 7. Comparison of the previous method and proposed method based on the GPs from Model 1 and Model 2 in Hassanzadeh test: (a) Characteristic element length, (b) stress–strain curves, and (c) locations of selected GPs.
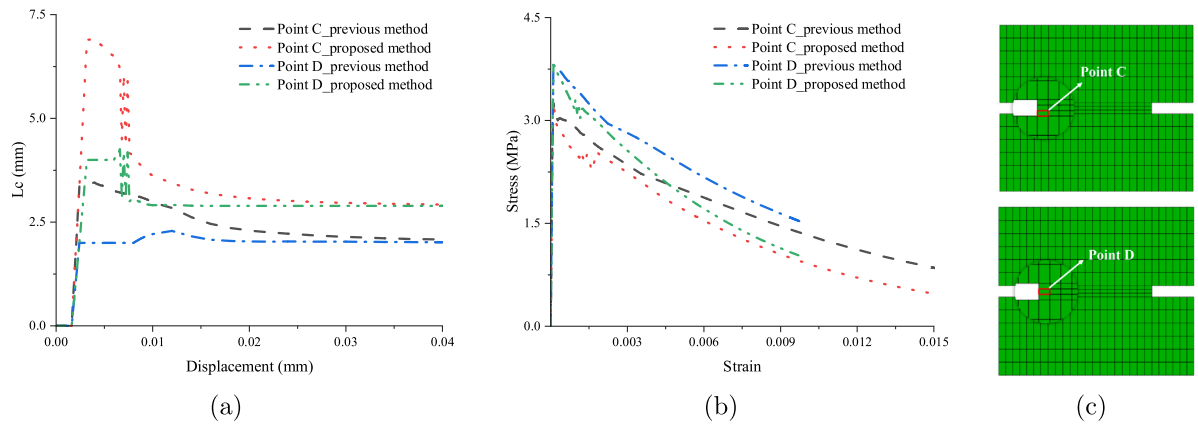
Fig. 8. Comparison of the previous method and proposed method based on the GPs from Model 3 in Hassanzadeh test: (a) Characteristic element length, (b) stress–strain curves, and (c) locations of selected GPs.
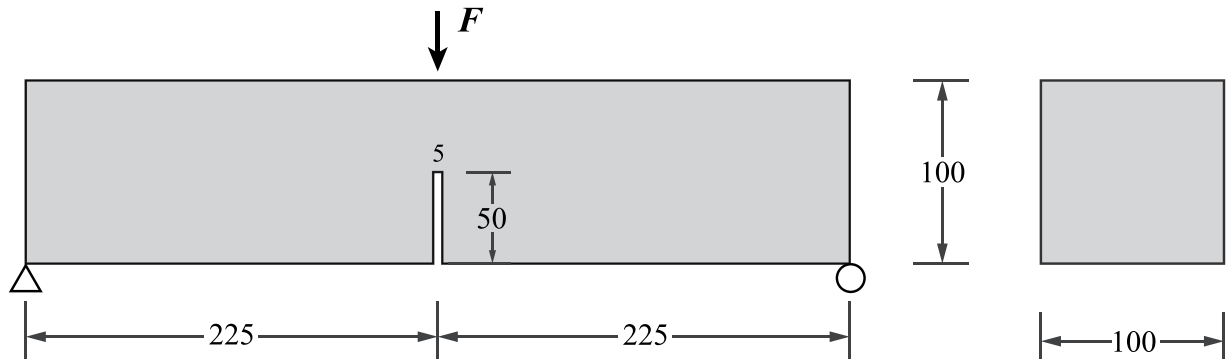
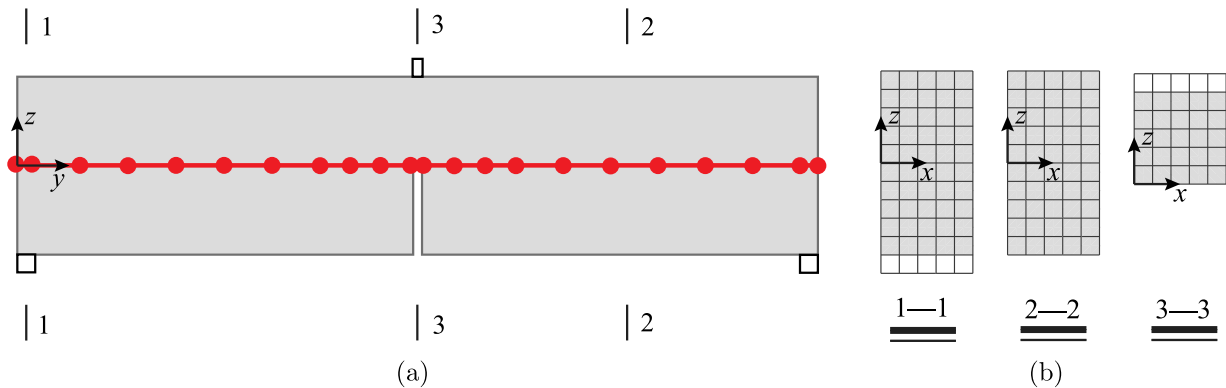**Fig. 9.** Geometric information and loading conditions of the TPB test.

Fig. 10. Discretization of (a) beam elements and (b) cross-sections for the TPB concrete beam.

Table 4
Model information of the notched TPB concrete beam.

Model No.	Model 1	Model 2	Model 3	Model 4	Model 5
Notch elements	1B2	1B4	1B3	2B3	3B3
Other elements	28B2	10B4	14B3	14B3	14B3
DoFs	21,318	23,694	21,747	22,605	23,463

simulations. Accordingly, three half cross-sections are discretized as shown in Fig. 10(b). The cross-sectional mesh comprises many nine-node quadratic Lagrange elements, each approximately 10 mm in size. The loading and support plates are represented by the white elements in Fig. 10(b). This study primarily investigates the impact of beam element discretization on structural response. Five distinct models, detailed in Table 4, employ varying beam element distributions. Models 1 and 2 are designed to test the proposed method's ability to replicate the performance of the previous method with B2 and B4 elements. The remaining models focus on examining the mesh-independent performance of the proposed method with B3 elements, particularly assessing the effect of varying numbers of B3 elements in the notch area.

Fig. 11 displays the reaction-load mid-span displacement curves derived from numerical models, employing both the previous and the proposed methods, alongside experimental data for comparison. As seen in Fig. 11(a), all models initially exhibit linear behavior consistent with the experimental results. Variations between Model 1 and Model 2 become apparent during the nonlinear phase, particularly in the softening branches, but their curves remain in agreement with experimental curves. These minor discrepancies may be attributed to the distinct approximations inherent to different beam elements. Conversely, Models 3 to 5, as demonstrated in Fig. 11(a), show higher peak loads and softening branches, reflecting the previous method's sensitivity to B3 elements. Nonetheless, the previous method can provide mesh-independent results regardless of the number of B3 elements implemented.

In Fig. 11(b), the numerical models display identical linear behaviors as observed earlier. Models 1 and 2 notably show consistent performance regarding peak loads and softening curves, replicating the results seen in Fig. 11(a). Minor discrepancies among the curves for Models 1, 2, and 3 are evident, which may be attributed to slight sensitivity to element order. Despite this, the curves from these three models closely approximate the experimental data, indicating that this sensitivity can be acceptable. In the analysis of mesh dependency with B3 elements, Model 5 exhibits a slightly lower softening curve beyond the 0.35 mm displacement, which deviate from the experimental data. This deviation might be linked to convergence issues stemming from the excessively fine beam element discretization in the notch. As discussed in [8], a finer mesh increases the potential combinations of loading and unloading at individual GP, complicating the numerical algorithm's task in determining the most accurate path. Despite this, Models 3 to 5 incorporating B3 elements match well with experimental data in Fig. 11(b), showing a significant improvement over their counterparts in Fig. 11(a). Therefore, the enhanced performance of B3 elements in these models, as provided by the proposed method, highlights its efficacy in achieving mesh-independent results.

Since damage mainly occurs around the notch, other beam sections are excluded in Fig. 12 to enhance the visualization of damage patterns. In the notch, damage consistently concentrates throughout the B2 element and on the left and right quarters of the B4 element. This pattern is observed with both the previous and proposed methods. However, with B3 elements, the previous method depicted in Fig. 12(c) shows damage extending beyond the central notch, resulting in an overestimated damage area. This overestimation leads to excessive fracture energy dissipation, contributing to the high softening curves of Model 3 (Fig. 11(a)). Although increasing the number of beam elements in the notch improves the damage distribution, as shown in Fig. 12(d), the outcome is still unacceptable.
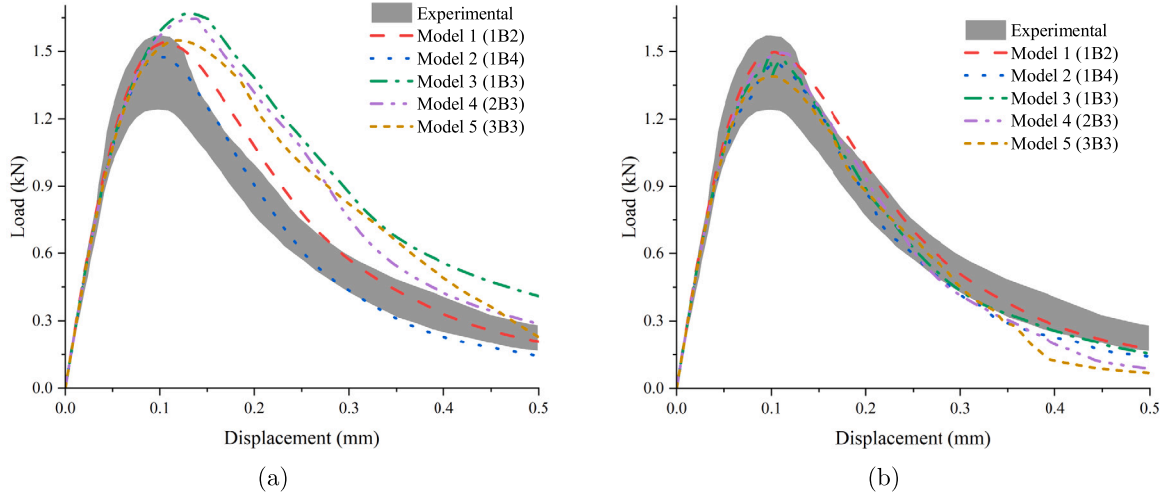
Fig. 11. Comparison of experimental and simulated load–midspan displacement curves from the TPB test: with (a) the previous method and (b) the proposed method.
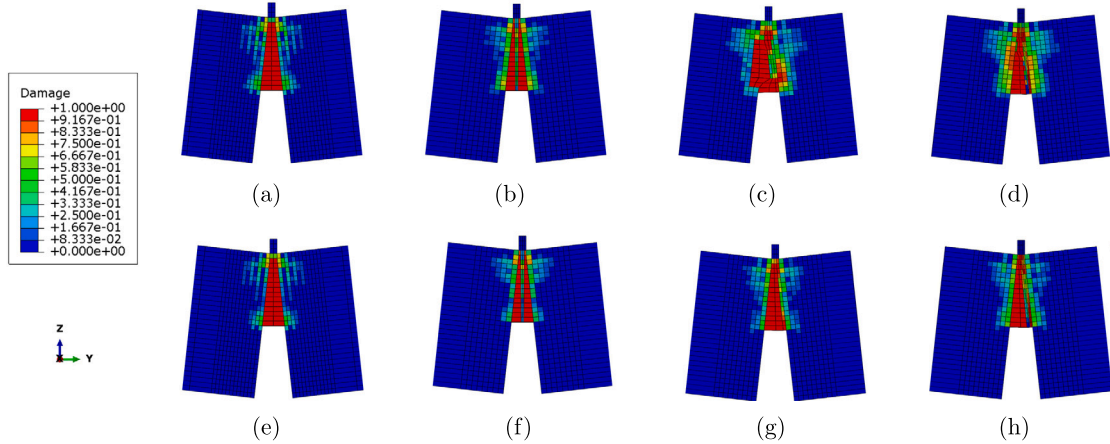

Fig. 12. Final damage distributions of the TPB concrete beam (deformed shape) with the previous method from: (a) Model 1 (1B2); (b) Model 2 (1B4); (c) Model 3 (1B3); (d) Model 4 (2B3) and new method from: (e) Model 1 (1B2); (f) Model 2 (1B4); (g) Model 3 (1B3); (H) Model 4 (2B3)

Conversely, Fig. 12(g) demonstrates the proposed method's ability to accurately predict the damage distribution that mainly occurs in two-thirds of a B3 element in the notch. This correct localization is also observed in Model 4 with two B3 elements, as shown in Fig. 12(h). These results demonstrate that the proposed method offers a more accurate estimation of the l_c, achieving a better regularization effect than the previous method.

5.3. The notched reinforced concrete panel

The third case is another uniaxial tension test on a reinforced concrete (RC) panel. The experimental test was conducted in [38] and considered a good benchmark for validating numerical simulations such as in [39]. The solution of a CUF-based 1D model for this problem has been validated in [40]. However, a different l_c calculation method was employed. In this part, the same example from [40] is selected to validate the proposed method for l_c in RC structures. Fig. 13 shows the loading layout and geometric information. This panel has double-edge notches with a width of 12.7 mm and a depth of 10 mm in the center. Three longitudinal rebars are distributed evenly along the panel height. One side of the panel is fixed, and the displacement control load with a maximum value of 0.8 mm is applied at the other end. The normal concrete is employed, and the corresponding material properties from [38] are listed in Table 5.

Table 5
Material properties of the notched RC panel.

Components	Properties	Symbols	Units	Values
Concrete	Young's modulus	E_c	GPa	27.349
	Poisson's ratio	v_c	–	0.175
	Mean compressive strength	f_{cm}	MPa	44
	Tensile strength	f_{ctm}	MPa	3.19
	Fracture energy	G_{ftm}	N/m	144
Steel	Young's modulus	E_s	GPa	191.584
	Poisson's ratio	v_s	–	0.28
	Yield strength	f_y	MPa	508

As suggested in [40], more beam element are assigned to the middle area close to the notch as shown in Fig. 14(a). However, the beam models from [40] only employed 5 and 7 B3 elements, which were validated in terms of load–displacement curves. The number of beam models may be too small to capture the correct damage distributions. Therefore, more beam elements are considered in this case to assess the mesh-independent performance of the proposed method. The models' information is listed in Table 6. The cross-sectional discretization is the same as in [40] as shown in Fig. 14(b). Multiple L9 are utilized for cross-sectional expansion. The Component-Wise (CW) approach is employed to independently consider the actual geometries and material properties of concrete and steel, in which no bond occurs. Lagrange points are placed at the boundary of steel and concrete to ensure
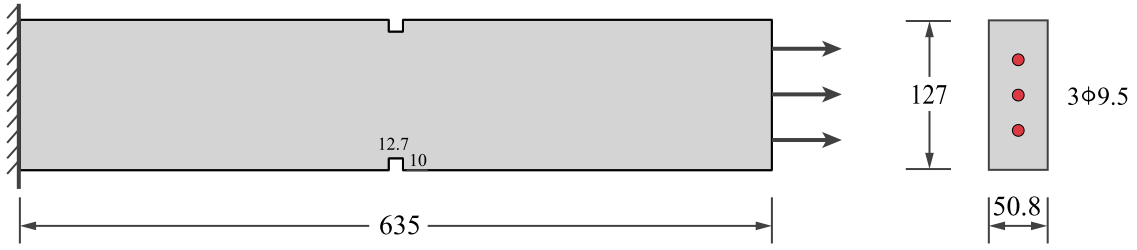
Fig. 13. Geometric information and loading conditions of the notched RC panel (Unit: mm).
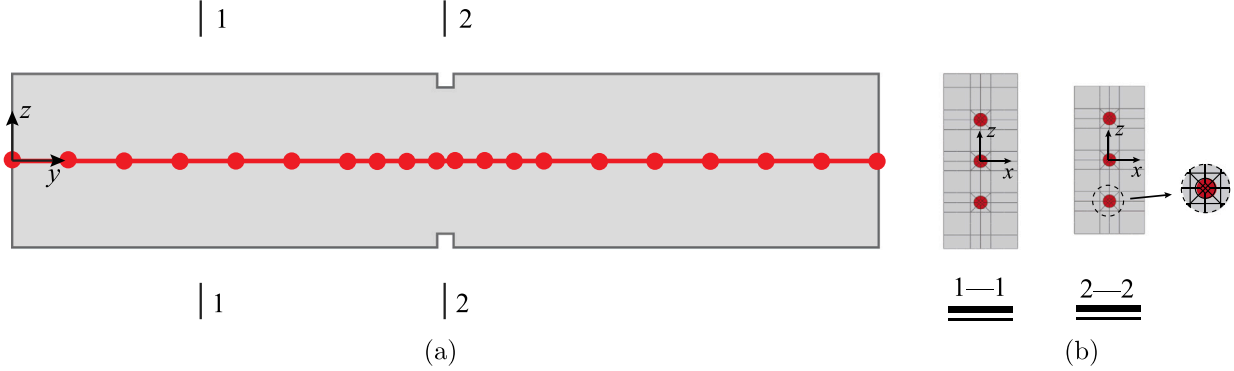

Fig. 14. Discretization of (a) beam elements and (b) cross-sections for the notched RC panel test.

Table 6
Model information of the notched RC panel.

Model No.	Model 1	Model 2	Model 3	Model 4
Beam elements	21B3	25B3	29B3	33B3
DoFs	53,685	63,693	73,701	83,709

Fig. 15. Comparison of experimental and simulated reaction load–displacement curves of the notched RC panel.

displacement continuity. More details about the CW approach can be found in [41]. Since the circle rebars occur, the discretization on the cross-section leads to the irregular shape, which is a good case for assessing the proposed l_c.

Fig. 15 shows the experimental and numerical load–displacement curves. The validation of mesh independency from the previous method is absent in this case. For comparative purposes, only the result from Model 2 with the method earlier is plotted in a black solid line in 15. The observed discrepancies between the linear parts of the numerical and experimental curves were explained in [40]. It is worth noticing that all numerical models present identical linear behaviors. A divergence in the softening curves between the numerical models employing the previous and proposed methods is expected. The relatively higher softening curve in Model 2, using the previous method, is attributed to its larger l_c estimation. Nevertheless, all numerical results align with the experimental range. This phenomenon may indicate that the previous method can provide a relatively accurate structural behavior for RC structures within an acceptable margin of error. Comparative analysis of different models using the proposed method reveals consistent, mesh-independent results, indicating the reliability of this proposed approach.

Fig. 16 presents final damage distributions from various numerical models. Evidently, the damage in Fig. 16(a) differs from that in Fig. 16(c). This difference is due to the different l_c calculation methods. From Fig. 16(b) to Fig. 16(e), it can be seen that the finer mesh provides more detailed damage distribution information. However, a common feature across these models is the presence of low damage intensity in areas between two major damage bands. This phenomenon occurs as these intermediate areas undergo unloading during damage localization. It is the same as the intact regions between
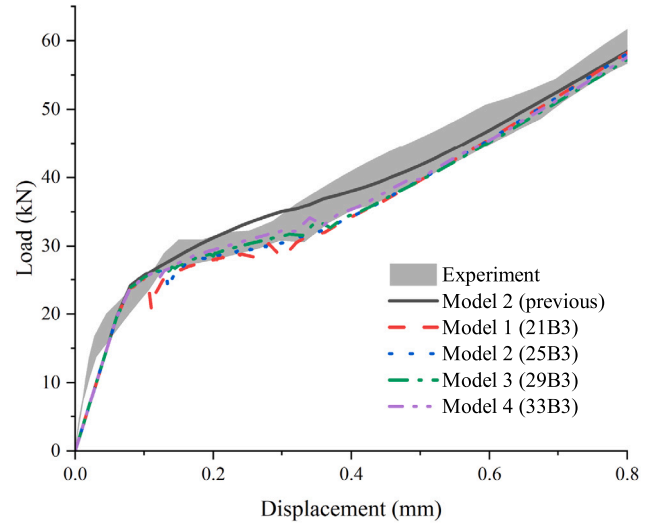
two cracks in experimental campaigns. Consequently, the unloading behavior observed between two damage bands can explain fluctuations observed among numerical curves with the proposed method in Fig. 15. Such fluctuations are absent in the model using the previous method, which is a potential shortcoming. These fluctuations lead to challenging convergence issues, which can be mitigated by reducing the step size, though this adjustment may require longer computational times.

6. Conclusions

This paper introduces an enhanced crack band model for the higher-order structural theories and beam elements based on CUF, aimed at mitigating the spurious size dependency of FE solutions. This model incorporates a refined method for estimating l_c, integrated into a
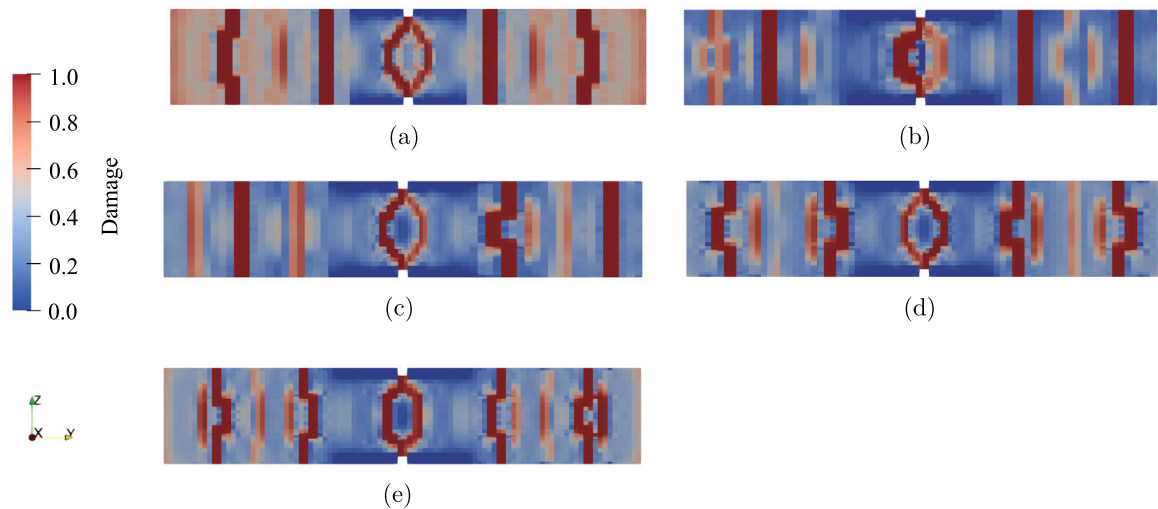
Fig. 16. Final damage distributions of the notched RC panel: (a) Model 2 using the previous method; (b) Model 1 (21B3); (c) Model 2 (25B3); (d) Model 3 (29B3); (e) Model 4 (33B3)

modified Mazars damage model. Three numerical examples involving concrete structures were analyzed to evaluate this method for estimating l_c. The comparison of experimental and numerical results leads to the following key conclusions:

(1) The use of higher-order structural theories and beam elements leads to the strain softening localized into parts of the element rather than the whole element. For instance, using B3 elements results in the localization of strain softening across approximately two-thirds of the element.

(2) Strain localization is observed in the material upon reaching a specific level of damage, leading to a reduction in crack bandwidth. This reduction is quantified by a specific parameter introduced in this study.

(3) The proposed method for estimating l_c can effectively identify whether strain softening has localized within parts of a beam element and provide an appropriate adjustment to l_c as needed. This approach enhances the objectivity of numerical models, achieving greater independency from mesh size and reducing sensitivity to element order.

(4) While the proposed method proves effective for plain concrete structures, it may encounter convergence challenges in reinforced concrete structures, potentially due to irregular mesh discretization in the cross-section.

In conclusion, the proposed method for calculating the characteristic element length l_c has been validated in tension-dominant, beam-like concrete structures using 1D CUF-based beam models. This calculation method offers a promising alternative for mitigating the issue of mesh dependency. Future studies will aim to investigate the adaptation of this method to 2D CUF-based plate or shell elements or 3D solid elements. Additionally, practical applications involving actual RC members, which present more complex and varied structural scenarios, will also be explored.

CRediT authorship contribution statement

J. Shen: Writing – original draft, Visualization, Software, Methodology, Investigation, Formal analysis, Data curation. **M.R.T. Arruda:** Writing – review & editing, Supervision, Investigation, Conceptualization. **A. Pagani:** Writing – review & editing, Resources, Project administration, Funding acquisition. **M. Petrolo:** Writing – review & editing, Project administration, Conceptualization.

Declaration of competing interest

The authors declare that they have no known competing financial interests or personal relationships that could have appeared to influence the work reported in this paper.

Data availability

The authors do not have permission to share data.

Acknowledgments

References

[1] Hofstetter B, Valentini G. Review and enhancement of 3D concrete models for large-scale numerical simulations of concrete structures. Int J Numer Anal Methods Geomech 2013;37(3):221–46.

[2] Mazars J. Application de la mécanique de l'endommagement au comportement non linéaire et à la rupture du béton de structure [Ph.D. thesis], Université Pierre et Marie Curie Paris 6; 1984.

[3] Mazars J. A model of a unilateral elastic damageable material and its application to concrete. In: Fracture toughness and fracture energy of concrete. Elsevier Science Publishers; 1986, p. 61–71.

[4] Berdichevsky V, Armanios E, Badir A. Theory of anisotropic thin-walled closed-cross-section beams. Compos Eng 1992;2(5–7):411–32.

[5] Lee J, Fenves G. Plastic-damage model for cyclic loading of concrete structures. J Eng Mech 1998;124(8):892–900.

[6] Wu J, Li J, Faria R. An energy release rate-based plastic-damage model for concrete. Int J Solids Struct 2006;43(3–4):583–612.

[7] Jirásek M. Mathematical analysis of strain localization. Rev eur génie civ 2007;11(7–8):977–91.

[8] Jirásek M. Nonlocal damage mechanics. Rev eur génie civ 2007;11(7–8):993–1021.

[9] Comi C. A non-local model with tension and compression damage mechanisms. Eur J Mech A Solids 2001;20(1):1–22.

[10] Simone A. Explicit and implicit gradient-enhanced damage models. Rev eur génie civ 2007;11(7–8):1023–44.

[11] Pijaudier-Cabot G, Bažant ZP. Nonlocal damage theory. J Eng Mech 1987;113(10):1512–33.

[12] Bažant ZP, Oh BH. Crack band theory for fracture of concrete. Matériaux et const 1983;16(3):155–77.

[13] Jirásek M, Bauer M. Numerical aspects of the crack band approach. Comput Struct 2012;110:60–78.

[14] Arruda M, Pacheco J, Castro LM, Julio E. A modified Mazars damage model with energy regularization. Eng Fract Mech 2022;259:108129.

[15] Rots JG. Computational modeling of concrete fracture [Ph.D. thesis], Delft, Netherlands: Delft University of Technology; 1988.

[16] Oliver J. A consistent characteristic length for smeared cracking models. Internat J Numer Methods Engrg 1989;28(2):461–74.

[17] Govindjee S, Kay GJ, Simo JC. Anisotropic modelling and numerical simulation of brittle damage in concrete. Int J Numer Methods Eng 1995;38(21):3611–33.

[18] Cervenka V, Pukl R, Ozbold J, Eligehausen R. Mesh sensitivity effects in smeared finite element analysis of concrete fracture. Fract Mech Concr Struct 1996;2:1387–96.

[19] He W, Xu Y, Cheng Y, Jia P-F, Fu T-T. Tension-compression damage model with consistent crack bandwidths for concrete materials. Adv Civ Eng 2019;2019.

[20] Slobbe A, Hendriks M, Rots J. Systematic assessment of directional mesh bias with periodic boundary conditions: Applied to the crack band model. Eng Fract Mech 2013;109:186–208.

[21] Carrera E, Giunta G, Nali P, Petrolo M. Refined beam elements with arbitrary cross-section geometries. Comput Struct 2010;88(5–6):283–93.

[22] Carrera E, Giunta G, Petrolo M. Beam structures: classical and advanced theories. John Wiley & Sons; 2011.

[23] Kaleel I, Petrolo M, Carrera E. Elastoplastic and progressive failure analysis of fiber-reinforced composites via an efficient nonlinear microscale model. Aerotecnica Missili Spazio 2018;97:103–10.

[24] Arruda M, Castro L, Ferreira A, Martins D, Correia J. Physically non-linear analysis of beam models using Carrera Unified Formulation. Compos Struct 2018;195:60–73.

[25] Shen J, Pagani A, Arruda M, Carrera E. Exact component-wise solutions for 3D free vibration and stress analysis of hybrid steel–concrete composite beams. Thin-Walled Struct 2022;174:109094.

[26] Pagani A, Carrera E, Augello R, Scano D. Use of Lagrange polynomials to build refined theories for laminated beams, plates and shells. Compos Struct 2021;276:114505.

[27] Pagani A, Carrera E, Scano D, Augello R. Finite elements based on Jacobi shape functions for the analysis of beams, plates and shells. Internat J Numer Methods Engrg 2023;124(20):4490–519.

[28] Nagaraj M, Reiner J, Vaziri R, Carrera E, Petrolo M. Progressive damage analysis of composite structures using higher-order layer-wise elements. Composites B 2020;190:107921.

[29] Nagaraj M, Reiner J, Vaziri R, Carrera E, Petrolo M. Compressive damage modeling of fiber-reinforced composite laminates using 2D higher-order layer-wise models. Composites B 2021;215:108753.

[30] Shen J, Arruda MT, Pagani A. Concrete damage analysis based on higher-order beam theories using fracture energy regularization. Mech Adv Mater Struct 2022;1–15.

[31] Shen J, Tiago Arruda MR, Pagani A. A consistent crack bandwidth for higher-order beam theories: Application to concrete. Int J Damage Mech 2023;10567895231215557.

[32] Shen J, Arruda M, Pagani A, Carrera E. A regularized higher-order beam elements for damage analysis of reinforced concrete beams. Mech Adv Mater Struct 2023;1–13.

[33] Carrera E, Petrolo M, Cinefra M, Zappino E. Finite element analysis of structures through unified formulation. Chichester, United Kingdom: John Wiley & Sons; 2014.

[34] Federation Internationale du Beton. Fib model code for concrete structures 2010. Lausanne, Switzerland: Ernst & Sohn; 2013.

[35] European Committee for Standardization. EN 1992-1-1 eurocode 2: Design of concrete structures - part 1-1: General ruels and rules for buildings. Brussels, Belgium: CEN, EN; 2005.

[36] Hassanzadeh M. Behaviour of fracture process zones in concrete influenced by simultaneously applied normal and shear displacements. Division of Building Materials, Lund Institute of Technology; 1992.

[37] Koermeling HA, Reinhardt HW. Determination of the fracture energy of normal concrete and epoxy modified concrete. Technical report 5-83-18, Stevin Lab, Delft University of Technology: Stevin Lab, Delft University of Technology; 1983.

[38] Ouyang C, Wollrab E, Kulkarni S, Shah S. Prediction of cracking response of reinforced concrete tensile members. J Struct Eng 1997;123(1):70–8.

[39] Drougkas A, Sarhosis V, Thermou G. Micromechanical homogenisation of steel bars in reinforced concrete for damage analysis. Mater Today Commun 2022;31:103235.

[40] Nagaraj MH, Maiaru M. Progressive damage analysis of steel-reinforced concrete beams using higher-order 1D finite elements. Int J Multiscale Comput Eng 2023;21(4).

[41] Carrera E, Augello R, Pagani A, Xu X. Component-wise approach to reinforced concrete structures. Mech Adv Mater Struct 2022;29(25):3871–88.